

Article

Effect of La on Microstructure, Mechanical Properties and Friction Behavior of In Situ Synthesized TiB₂/6061 Composites

Jing Jia , Weibin Zhuang *, Jinghui Li, Qing Cao and Jingfu Liu

School of Materials Science and Engineering, Liaoning Technical University, Fuxin 123000, China

* Correspondence: zhuangweibin@lntu.edu.cn

Abstract: In situ synthesized 3 wt.%TiB₂/6061 composites with different La contents were fabricated by an Al-K₂TiF₆-KBF₄ system at 850 °C with ball milling and stirring casting. The effects of La content (0 wt.%, 0.1 wt.%, 0.3 wt.%, 0.5 wt.%) on the microstructures and mechanical properties of the composites at room temperature were investigated. The results showed that the addition of La could refine α -Al grains and modify the morphology of TiB₂ particles significantly. In 0.3 wt.%La-3 wt.%TiB₂/6061 composites, there are chamfering planes on the surface of TiB₂ particles, which are caused by the adsorption of La on the {11 $\bar{2}$ 0}, {1 $\bar{2}$ 12} and {10 $\bar{1}$ 1} crystal planes. The values of YS, UTS and EL of the composites with 0.3 wt.% La were 216.8 MPa, 273.0 MPa and 11.2%, which were 69.2%, 34.8% and 5.7% higher than those of the 3 wt.%TiB₂/6061 composites. The improvement of mechanical properties was mainly attributed to the grain refinement, distributed particles and transformation of particle morphology. In friction behavior, 0.3 wt.%La-3 wt.%TiB₂/6061 composites have the best wear resistance properties with the smallest and shallowest grooves on the surface after wearing. The main mechanisms of the composites are adhesive wear and abrasive wear. In summary, the best content of La addition in 3 wt.%TiB₂/6061 composites is 0.3 wt.%.

Keywords: in situ synthesized; TiB₂/6061; La; microstructure; mechanical properties; friction behaviors



Citation: Jia, J.; Zhuang, W.; Li, J.; Cao, Q.; Liu, J. Effect of La on Microstructure, Mechanical Properties and Friction Behavior of In Situ Synthesized TiB₂/6061 Composites. *Metals* **2024**, *14*, 1169. <https://doi.org/10.3390/met14101169>

Academic Editors: Roberto Martínez Sánchez, Sergio Gonzalez Sanchez and Carlos G. Garay Reyes

Received: 9 September 2024
Revised: 28 September 2024
Accepted: 8 October 2024
Published: 14 October 2024



Copyright: © 2024 by the authors. Licensee MDPI, Basel, Switzerland. This article is an open access article distributed under the terms and conditions of the Creative Commons Attribution (CC BY) license (<https://creativecommons.org/licenses/by/4.0/>).

1. Introduction

Aluminum alloys and aluminum matrix composites are two of the most promising lightweight structural materials in the manufacturing and aerospace industries because of their low cost, light weight and high specific strength and stiffness [1,2]. In situ synthesized TiB₂ particles are characterized by high hardness, high elastic modulus, excellent chemical stability, corrosion resistance and good interfacial wettability, which make them ideal strengthening phases in composites [3,4].

However, in situ synthesized TiB₂ particles have large surface energy for agglomeration, affecting the improvement of mechanical properties of TiB₂/Al composites [5,6]. The mechanical properties of composites are closely related to their microstructures. Therefore, it is crucial to develop a new strategy for optimizing the microstructures of the composites, such as preventing TiB₂ particle agglomeration by weakening the edges and corners of particles, so to create better performances in mechanical behaviors [7,8]. Microstructures can be effectively optimized by ultrasonic vibration [9,10], electromagnetic intervention [11,12] and mechanical stirring during the preparation process [13,14]. Nevertheless, the drawbacks of these techniques are higher costs and more complex processes.

It has been reported that the addition of alloying elements in in situ synthesized TiB₂/Al composites may cause microstructure evolution and mechanical property improvement [15,16]. Zhang et al. [17], who adopted a combination of first principles calculations and experimental investigation, reported that Sc can greatly refine TiB₂ particle size, optimize particle distribution and transform particle morphologies from hexagonal disks to spheres. Sc can also lead to the formation of coarse TiB₂ particles and promote growth on the {0001} crystal plane [18].

Sun et al. [19] explored the effect of Cu on the transformation of TiB₂ particles via multi-scale microstructure characterization and statistics. They discovered that Cu was preferentially adsorbed on the {10 $\bar{1}$ 1} crystal plane of the TiB₂ particles, due to the small aspect ratio of the TiB₂ particles. Zhang et al. [20] fabricated in situ 50 vol.% TiB₂/Al composites with Cu and Zn via an Al-Ti-B system, which effectively improved the microstructures and mechanical properties of the composites, because Cu and Zn can inhibit reaction temperatures. Xue et al. [21] fabricated 5 wt% TiB₂/A356 composites with CeO₂, revealing that Ce can improve TiB₂ particle agglomeration, reduce the size of α -Al grains and change the morphology of eutectic Si. The addition of trace CeO₂ also helps to improve the elongation of composites. In our previous work [22], we elaborated the mechanism of trace Mn addition in TiB₂/Al composites and described the process of Mn in particle morphology evolution and in the alleviation of particle agglomeration.

La is a typical rare earth element with active chemical properties, low potential and a special electronic layer arrangement. La can reduce the porosity of aluminum alloys, reduce inclusions and purify harmful elements, thus improving the strength of alloys. Trace La addition can refine the grain size and enhance the strength of an Al-Mg-Si alloy [23]. Tsai et al. [24] proved that La decreased the eutectic nucleation and growth temperatures in A356 alloys. Zheng et al. [25] found that La can refine grain size from 500 μ m to 100 μ m in an Al-Si alloy. La also significantly promoted the formation of the multiple Si twins, and the average length of the eutectic Si particles decreased by 48.25%.

In this work, we systematically investigated the effects of different La contents on the microstructure, mechanical properties and friction behaviors of 3 wt.% TiB₂/6061 composites in T6 conditions. The effect of La on grain size, particle morphology, mechanical properties and friction behaviors was examined.

2. Materials and Methods

The 6061 aluminum alloy was selected as the matrix for the composites. The chemical composition of the 6061 aluminum alloy in this work is listed in Table 1. In order to synthesize the TiB₂ particles in situ, K₂TiF₆ powder and KBF₄ powder were chosen as raw materials, both of them with a purity of 98 wt.%. La₂O₃ powder (analytical reagent) was produced by Kernel in Tianjin, China.

Table 1. Chemical composition of 6061 aluminum alloy in this work (wt.%).

Element	Si	Cu	Mn	Mg	Zn	Ti	Fe	Al
Content	0.5	0.3	0.15	1.0	0.25	0.15	0.7	96.95

The mole ratio of K₂TiF₆ powder and KBF₄ powder is 1:2, which corresponds to the fabrication of 3 wt.% TiB₂/6061 composites. The contents of added La were 0 wt.%, 0.1 wt.%, 0.3 wt.% and 0.5 wt.%, respectively. K₂TiF₆ powder, KBF₄ powder and La₂O₃ powder were mixed using a planetary ball mill machine with a ZrO₂ (d = 8 mm)-ball-to-powder weight ratio of 10:1 and was milled at 300 rpm/min for 5 h. Figure 1 shows the powder morphology before and after ball milling. The average particle size in the mixture was 10 μ m (Figure 1d). As can be seen in the magnification, La₂O₃ powder adhered to K₂TiF₆ powder and KBF₄ powder uniformly (Figure 1e,f). The mixture was divided into equal masses, wrapped in aluminum foil, and heated at 200 °C for 2 h to thoroughly remove moisture. The 6061 alloy was heated in a graphite crucible placed in an electrical resistance furnace until it had melted [26]. The mixture was added to the melted alloy at 850 °C under mechanical stirring (150 rpm/min for 1 h). The slag was decanted, and then the melt was cast into a graphite mold (preheated at 300 °C). The as-cast ingots were subjected to T6 heat treatment: solution treatment (540 °C, 90 min), cold water quenching, artificial aging (180 °C, 18 h).

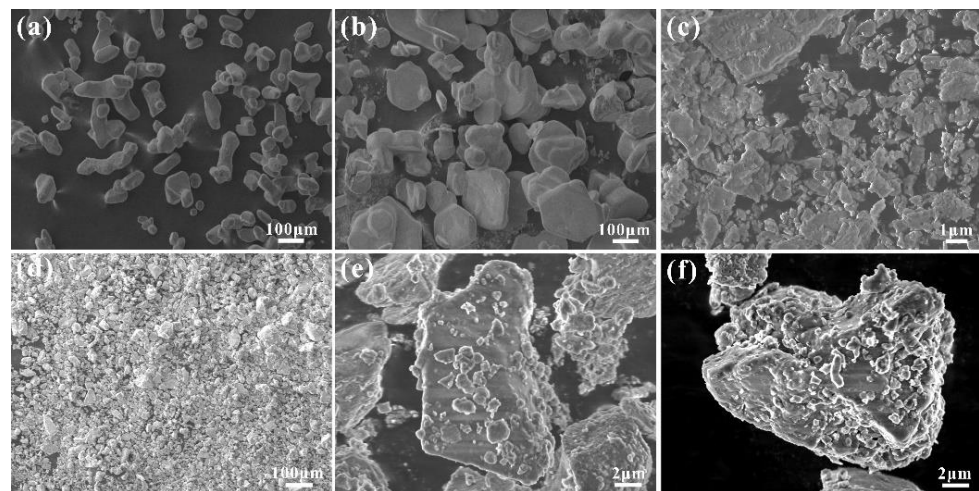


Figure 1. Raw material powder morphology: (a) KBF_4 ; (b) K_2TiF_6 ; (c) La_2O_3 ; (d) mixture after ball milling; (e,f) magnification of the mixture.

According to the international metallographic preparation procedure, the metallographic samples were polished and etched with Keller's reagent. Phase identification of the composites was performed by XRD-6100 X-ray diffraction (XRD, Shimadzu, Kyoto Japan). The microstructure of the samples was observed with a JSM-7500F field emission scanning electron microscope (SEM, JEOL, Tokyo, Japan). Yield strength (YS), ultimate tensile strength (UTS) and elongation (EL) were tested by a CMT-5105 electronic tensile testing machine (SANS, Shenzhen, China) at room temperature; five samples of each type were tested, and the average values were reported. The size of samples for tensile testing is shown in Figure 2. The fracture morphology of the tensile samples was observed by SEM. Wear resistance was tested by an HSM-TRB ball disc wear testing machine (CSM, Graz, Austria); the wear pair was a GCr15 steel ball ($\Phi 6$ mm, 870 HV, $R_a = 0.8$), the speed of the wearing test was 5000 rpm and the applied load was 500 N, with a single wearing time of 30 min. An OLS-4000 laser confocal microscope (LCM, OLYMPUS, Tokyo, Japan) was used to observe the surface of the composites after wearing. The hardness of the composites was tested by an HBS-3000 Brinell hardness tester (Fangyuan, Jinan, China); for each sample, ten points were chosen for testing, and the average value was considered as the hardness of the composites.

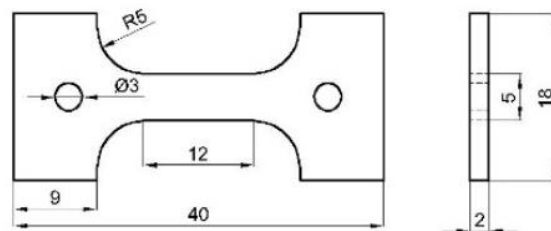


Figure 2. The size of samples for tensile property testing (mm).

All first-principle calculations in this work were performed using density functional theory (DFT) by Cambridge Serial Total Energy Package (CASTEP) in Materials Studio (MS) software (2020 version). The Perdew Burke Ernzerhof (PBE) functional in Generalized Gradient Approximation (GGA) was used to calculate the exchange-related energy functional; the value of the plane-wave kinetic cutoff energy was set to 450 eV. A Monkhorst Pack grid of $(5 \times 5 \times 1)$ k-point was used in all calculations. To avoid interactions between top and bottom surfaces, the thickness of the vacuum layer was chosen to be 15 Å. The adsorption energy of La atoms on the surface of TiB_2 particles is defined as follows [27]:

$$E_{ads} = E_{\text{La}/\text{TiB}_2} - E_{\text{TiB}_2} - E_{\text{La}} \quad (1)$$

where E_{ads} is the adsorption energy of the surface (eV), E_{La/TiB_2} is the energy of the surface adsorption system (eV), E_{TiB_2} is the energy of the TiB_2 substrate (eV), E_{La} is the energy of isolated La atoms. In general, if E_{ads} shows a positive value, it indicates that the adsorption process is an endothermic process. In the comparison of adsorption energy, it is considered that an exothermic process (negative value) is more favorable than an endothermic process (positive value) because an exothermic process represents stronger interaction.

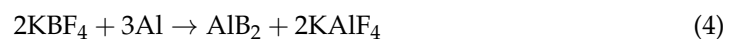
3. Results and Discussion

3.1. Phase Analysis

An Al-KBF₄-K₂TiF₆ system was used to synthesize TiB₂/6061 composites in situ. The reaction system was a closed, multi-component, constant pressure system, and the Gibbs free energy (ΔG) value can be used as a criterion for whether the reaction can spontaneously proceed. When $\Delta G < 0$, it is considered that the reaction can spontaneously and irreversibly proceed. The reaction in the Al-KBF₄-K₂TiF₆ system was as follows [28]:



In the actual reaction process, the above general reaction equation can be further divided into three stages:



Combining Equations (3) and (4), it can be found that Al₃Ti and AlB₂ may be synthesized during the reaction, which may cause a negative effect on the mechanical properties of the composites. According to Equation (5), it is possible for Al₃Ti and AlB₂ phases to react and spontaneously synthesize TiB₂ phases. When the ΔG value of Equation (5) was calculated, it resulted that if the reaction temperature rises above 680 °C, the reaction of Equation (5) would spontaneously proceed. In this work, the experimental temperature was set at 850 °C; there would only be TiB₂ particles in the composites in theory. Figure 3 shows the XRD pattern of 3 wt.%TiB₂/6061 composites with different La contents. It proved that the 3 wt.%TiB₂/6061 composites were mainly composed of Al and TiB₂ phases, and no peaks of AlB₂ and TiAl₃ could be observed, which was consistent with the ΔG value calculation results of the system. As for La, adding La₂O₃ to the 6061 melt caused the following reaction:

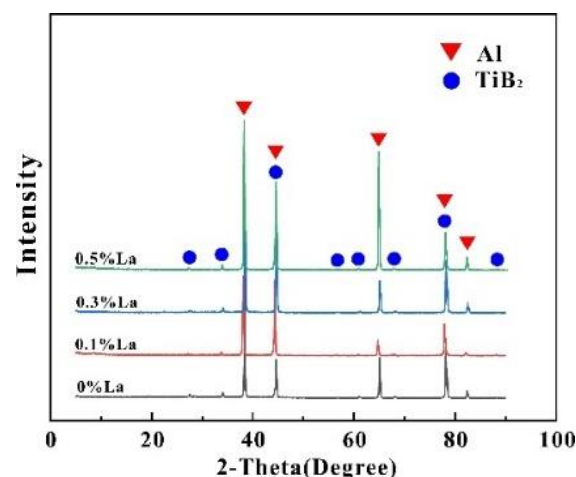
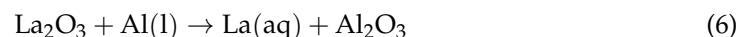


Figure 3. XRD pattern of 3 wt.%TiB₂/6061 composites with different La contents.

Therefore, La_2O_3 exhibits the same function as La. However, due to the maximum content of La being 0.5 wt.%, which did not reach the minimum detection limit of the device, no peaks containing La could be detected.

3.2. Microstructures of Composites with Different La Additions

Figure 4 shows the microstructure of 3 wt.% TiB_2 /6061 composites with different La contents. In 3 wt.% TiB_2 /6061 composites, the average size of α -Al grains was about 150 μm (Figure 4a). It can be observed that there was a large number of TiB_2 particle agglomerations on the grain boundaries and inside α -Al grains. In 0.1 wt.%La-3 wt.% TiB_2 /6061 composites, the size of α -Al grains slightly decreased, with an average grain size of about 90 μm (Figure 4b). When the content of La was 0.3 wt.%, the average grain size was about 50 μm , as shown in Figure 4c. Meanwhile, the size and number of particle agglomerations were obviously reduced, with particles uniformly distributed along the grain boundaries. However, with 0.5 wt.% La addition, there were large-size dendrites, and the α -Al grain size was more than 200 μm , which was larger than that of the 3 wt.% TiB_2 /6061 composites.

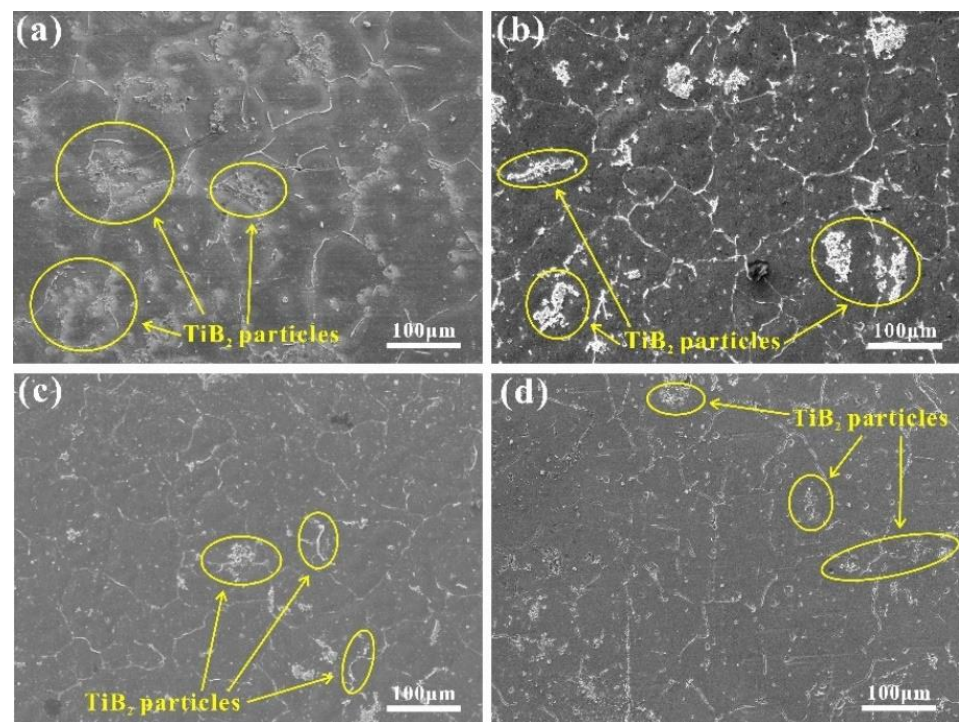


Figure 4. Microstructures of 3 wt.% TiB_2 /6061 composites with different La contents: (a) 0 wt.% La; (b) 0.1 wt.% La; (c) 0.3 wt.% La; (d) 0.5 wt.% La.

SEM images of TiB_2 particle distribution in the composites with different La contents are shown in Figure 5. It was found that La not only reduced the particle size but also significantly alleviated particle agglomeration because La could reduce the surface tension of the melt and improve the diffusion ability and wettability of TiB_2 particles in the melt. With La contents increasing from 0 wt.% to 0.3 wt.%, the size of particle agglomerations was obviously reduced, and more uniform particles could be observed. The 0.3 wt.% La addition generated the greatest effect on alleviating particle agglomeration. However, more serious particle agglomeration existed in the composites with 0.5 wt.% La, which may have been caused by rare earth inclusions forming, which reduced the wettability between TiB_2 particles and the matrix.

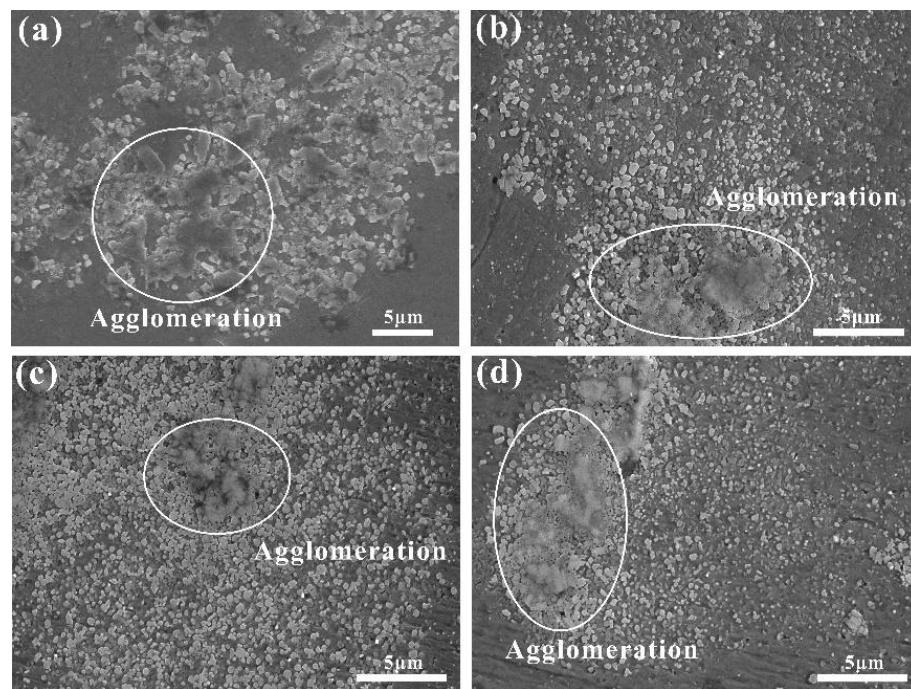


Figure 5. SEM images of TiB_2 particle distribution in the composites with different La contents: (a) 0 wt.% La; (b) 0.1 wt.% La; (c) 0.3 wt.% La; (d) 0.5 wt.% La.

3.3. Mechanical Properties of Composites with Different La Additions

Figure 6 shows the effect of La contents on the tensile properties of 3 wt.% TiB_2 /6061 composites. The tensile property of 0.3 wt.%La-3 wt.% TiB_2 /6061 composites was the best in all groups, as shown in Figure 6a. Compared with 3 wt.% TiB_2 /6061 composites, the YS and UTS increased by 69.2% and 34.8%, and the EL increased by 5.7%. As the content of La reached 0.5 wt.%, the tensile property of the composites sharply decreased, becoming even worse than that of 3 wt.% TiB_2 /6061 composites. The increasing trend of EL is consistent with the increasing trend of YS and UTS in Figure 6b, which indicates that trace La addition contributed to strength–ductility synergism. It has been mentioned before that La can promote grain size refinement, so the deformation was more dispersed, and the uniformity was improved. The cracking risk caused by stress concentration was decreased, which can allow more deformation and exhibit high ductility. Meanwhile, it could not be ignored that grain boundaries could obstruct crack propagation and absorb more energy in the fracture process.

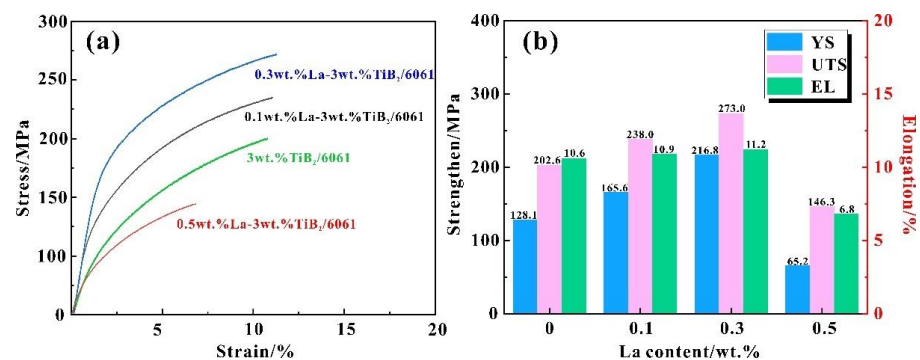


Figure 6. Effect of La contents on the tensile property of 3 wt.% TiB_2 /6061 composites: (a) typical stress–strain curves, (b) average tensile strength and elongation.

Figure 7 shows the fracture morphologies of the composites with different La contents. There were many dimples at the fracture of the composites, which proved irreversible plastic deformation occurred in the composites, a typical fracture with micropore aggregation. With La contents increasing from 0.1 wt.% to 0.3 wt.%, the size of dimples was increased and deepened. The size of dimples was mostly determined by the micropore nucleation number and the plasticity of the composites. The fracture morphologies were well consistent with the tensile property. Furthermore, there were TiB_2 particles at the bottom of the dimples; it could be confirmed that TiB_2 particles were well bonded with the 6061 alloy [29,30].

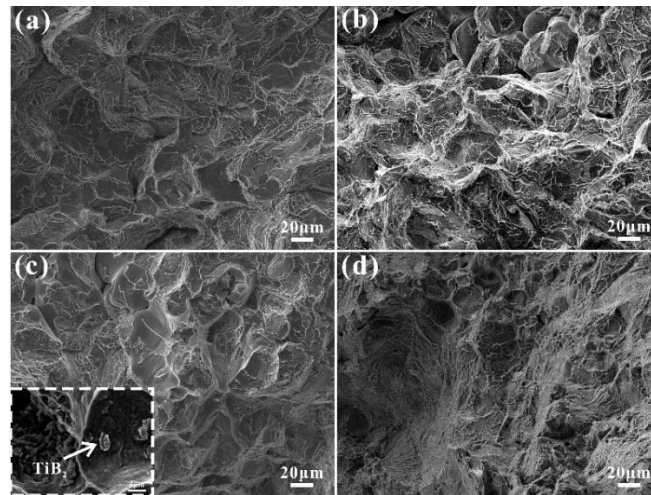


Figure 7. Fracture morphologies of the composites with different La contents: (a) 0 wt.% La; (b) 0.1 wt.% La; (c) 0.3 wt.% La; (d) 0.5 wt.% La.

3.4. Friction Behaviors of Composites with Different La Additions

Figure 8 shows the friction coefficient curves of the composites with different La contents. The friction coefficient curves fluctuated over time within the range of 0.4~0.9. The average friction coefficient of 3 wt.% TiB_2 /6061 composites was 0.524, with intense fluctuations and multiple peaks and valleys on the curves (Figure 8a). Because of the large difference between TiB_2 particles and the 6061 alloy in hardness, the degree of curve fluctuation depended on the distribution of TiB_2 particles. The particle agglomeration caused intense fluctuations on the curves at the beginning of wearing. As the wearing continued, the agglomeration detached, and the curve fluctuations gradually decreased. The average friction coefficient of the composites with 0.1 wt.% La and 0.3 wt.% La tended to decrease, with smoother fluctuation (Figure 8b,c). The composites with 0.5 wt.% La showed a larger average friction coefficient than the composites without La addition. The composites with 0.3 wt.% La have the best wear resistance.

Figure 9 shows the typical surface morphologies of the composites after wearing. The surface morphologies of the composites are mainly composed of grooves and pits after wearing. The grooves are the strip-shaped lines on the surface, which were caused by the friction between the wear pair and the wear surface under load. The depth and size of grooves can intuitively reflect the wear resistance of the composites. During the wear test, TiB_2 particle agglomerations separated from the composites and left pits on the surface. As shown in Figure 9, the grooves of the 0.3 wt.%La-3 wt.% TiB_2 /6061 composites were the smallest and shallowest, with fewer pits. Figure 10 shows the plane fitting of the deepest section after the wearing of the composites with different La contents, expressing the surface roughness. Height difference gaps existed in the 3 wt.% TiB_2 /6061 composites, indicating poor wear resistance (Figure 10a). With La contents increasing from 0.1 wt.% to 0.3 wt.%, the surface height difference significantly decreased (Figure 10b,c). The pits on the surface of 0.5 wt.% La-3 wt.% TiB_2 /6061 composites were the deepest (Figure 10d). The

results of the surface morphologies were consistent with the friction coefficient curves of the composites.

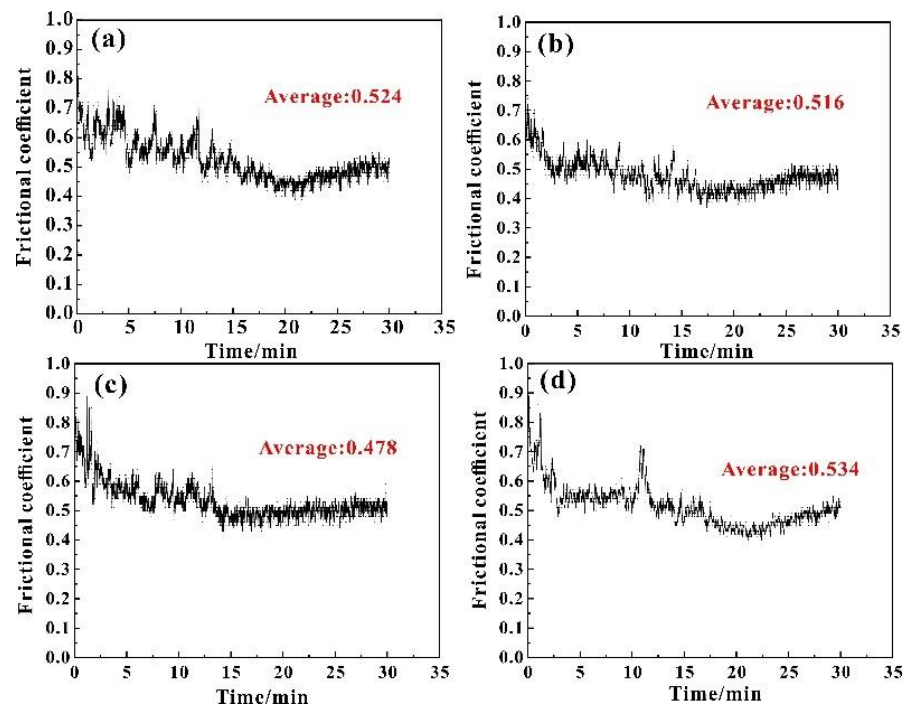


Figure 8. Friction coefficient curves of the composites with different La contents: (a) 0 wt.% La; (b) 0.1 wt.% La; (c) 0.3 wt.% La; (d) 0.5 wt.% La.

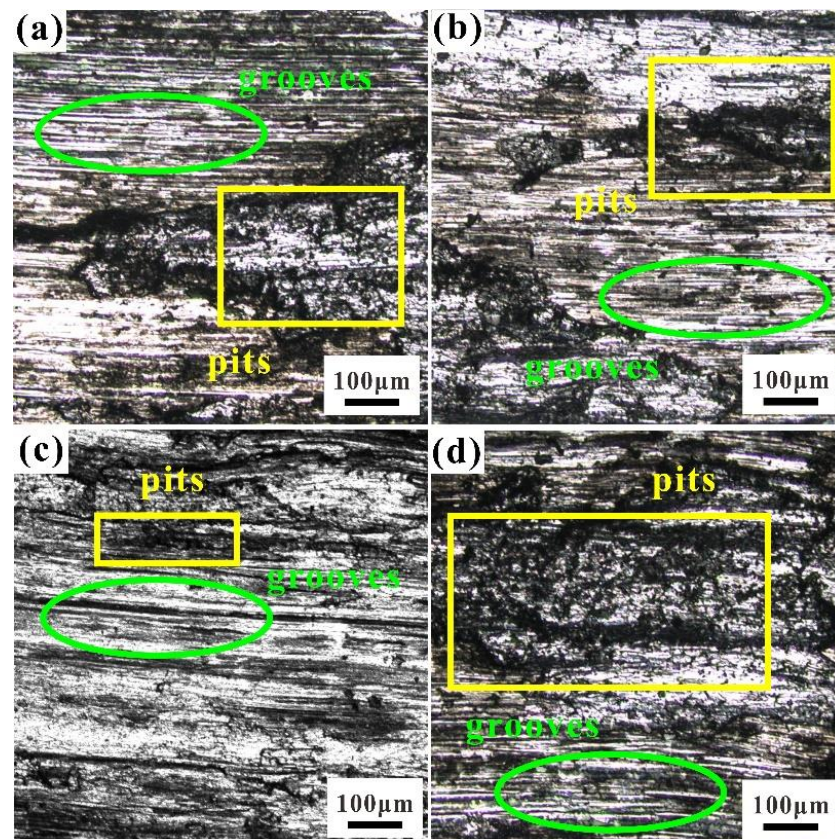


Figure 9. Typical surface morphologies after wearing of the composites with different La contents: (a) 0 wt.% La; (b) 0.1 wt.% La; (c) 0.3 wt.% La; (d) 0.5 wt.% La.

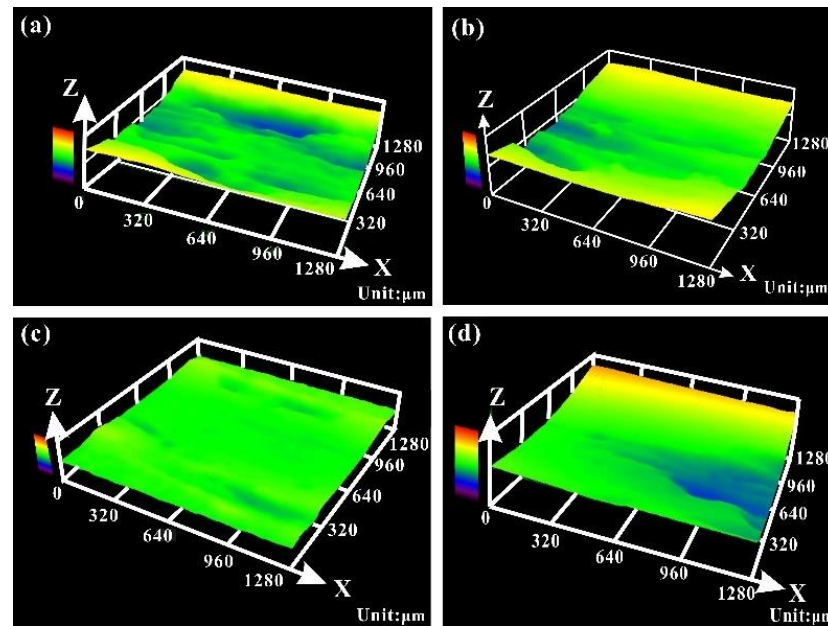


Figure 10. Plane fitting of the deepest section after wearing of the composites with different La contents: (a) 0 wt.% La; (b) 0.1 wt.% La; (c) 0.3 wt.% La; (d) 0.5 wt.% La.

4. Discussion

4.1. Microstructures

It is obvious that trace La addition could refine α -Al grains in 3 wt.%TiB₂/6061 composites. Aluminum has a face-centered cubic structure, and La has a hexagonal close-packed structure, so the solid solubility of La in the 6061 alloy is very small. During the solidification process, La would be enriched at the front of the solid–liquid interface, causing a continuous increase in the concentration gradient of liquid phases near the interface. The actual supercooling degree was much higher than the critical supercooling degree required for nucleation, which is known as the constitutional supercooling phenomenon. During the crystallization process, the grain size is mainly controlled by the ratio of nucleation rate and growth rate. With the increase in undercooling, the ratio of the nucleation rate to the growth rate increased, so the grain size significantly decreased. However, 0.5 wt.% La addition may lead to the formation of rare earth inclusions, having adverse effects on grain refinement. Rare earth inclusions are a potential threat for composites in a stress state. In addition, the α -Al grain size in the composites is much smaller than that of the 6061 alloy. This is attributed to the heterogeneous nucleation function of TiB₂ particles in the composites. Moreover, La can alleviate TiB₂ particle agglomeration and increase effective nucleation sites for grains, which also has a positive effect on grain size refinement.

In order to investigate the effect of La on TiB₂ particle morphologies, the 0.3 wt.%La-3 wt.%TiB₂/6061 composites were selected as the observation object. Figure 11 shows the microstructure details of TiB₂ particles. The lattice structure and atomic arrangement on each crystal plane of TiB₂ particles are shown in Figure 11a. According to crystallographic principles, the crystal plane with the smallest surface energy has the lowest growth rate and ultimately will be the main exposed crystal plane of the crystal. The ranking of crystal growth rates is as follows: $\{0001\} < \{10\bar{1}0\} < \{10\bar{1}1\} < \{11\bar{2}0\} < \{1\bar{2}12\}$. Therefore, TiB₂ particles exhibited regular hexagonal prism morphology wrapped by $\{0001\}$ and $\{10\bar{1}0\}$ crystal planes in 3 wt.%TiB₂/6061 composites. This has been proved in our previous works [22,26].

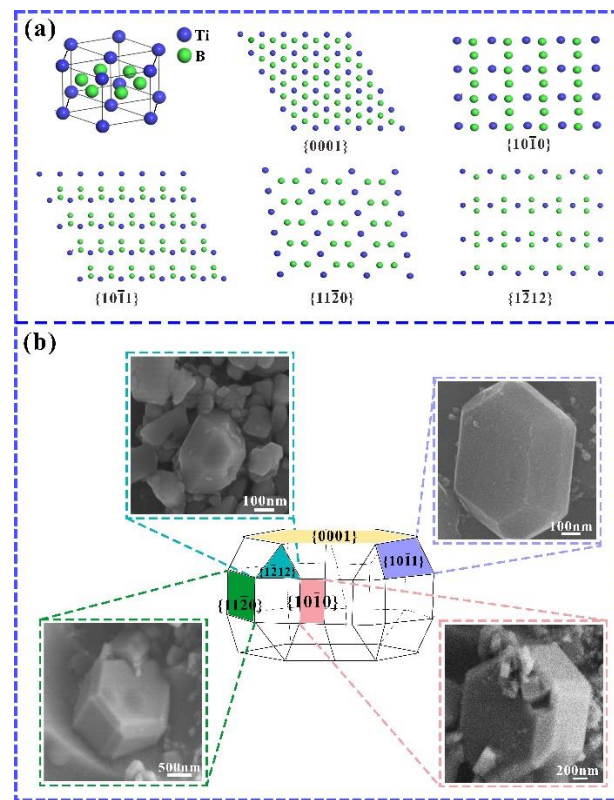


Figure 11. Microstructure details of TiB₂ particles: (a) lattice structure and atomic arrangement on each crystal plane of TiB₂ particles; (b) TiB₂ particles in the 0.3 wt.%La-3 wt.%TiB₂/6061 composites and schematic diagram of crystal structure.

It can be clearly observed in Figure 11b that the overall morphologies of TiB₂ particles still maintain hexagonal prisms, but multiple chamfering platforms appear on different planes. La can improve the fluidity of the solid–liquid interface and accelerate the speed of lattice orientation arrangement. So, the speed of crystal transformation is also accelerated. Most TiB₂ particles exhibited final morphologies in which narrow chamfering planes replaced the original edges. La adsorbed on different crystal planes of TiB₂ particles, which inhibited the degradation of the corresponding crystal planes and led to chamfering planes on the crystal surface. Table 2 shows the adsorption energy of La on different crystal planes of TiB₂ particles. The adsorption energies of La on {1120}, {1212} and {1011} crystal planes have negative values. The growth on these crystal planes was seriously inhibited, which maintained a lower energy state and eventually kept chamfering planes in the final morphology of TiB₂ particles.

Table 2. The adsorption energy of La on different crystal planes of TiB₂ (eV).

Crystal planes	{0001}	{1010}	{1011}	{1120}	{1212}
Adsorption energy	−1.1681	−0.7263	−0.5195	−3.2306	−0.5545

4.2. Strengthening Mechanisms

The improvement of the tensile property for 3 wt.%TiB₂/6061 composites can be attributed to grain refinement strengthening (σ_{GR}), Orowan strengthening (σ_{Orowan}) and thermal expansion coefficient mismatch strengthening (σ_{CTE}). The three strengthening mechanisms have been coupled by the following equation:

$$\Delta\sigma = \Delta\sigma_{GR} + ((\Delta\sigma_{Orowan})^2 + (\Delta\sigma_{CTE})^2)^{1/2} \quad (7)$$

The well-known Hall–Petch formula describes the relationship between YS and grain size [26,31]:

$$\sigma_{GR} = \sigma_0 + kd^{-1/2} \quad (8)$$

where σ_0 is the original YS of the alloy (MPa), k is a constant related to the composites, d is the average grain size of the composites (mm). It can be observed that grain refinement strengthening is negatively correlated with the grain size. With 0.3 wt.% La addition, the degree of grain refinement was the highest, and there would be more grain boundaries inhibiting dislocation movement.

If the composites were subjected to external forces, the interaction between moving dislocations and TiB₂ particles would produce Orowan strengthening. TiB₂ particles have high hardness, making it difficult for dislocations to cut through the composites. The general equation can be given as follows [32]:

$$\Delta\sigma_{Orowan} = \frac{2Gb}{D\left(\frac{\pi}{6V_p}\right)^{1/3}} \quad (9)$$

where G is the shear modulus of the composites (GPa), b is the Burgers vector of the composites (nm), D is the average size of TiB₂ particles (nm), V_p is the volume fraction of the particles (%). The Orowan strengthening mechanism reveals that the YS improvement of the composites is mainly due to the uniform distribution of TiB₂ particles and the decrease in particle size.

Thermal expansion coefficient (CTE) mismatch strengthening is produced by the CTE mismatch between TiB₂ particles and the 6061 alloy. CTE mismatch caused an increase in the dislocation density in deformation and dislocation tangled on the grain boundaries. The contribution of CTE strengthening in the composites can be presented by the following equation [33]:

$$\Delta\sigma_{CTE} = 1.25G_m b / \sqrt{\frac{12(T_m - T_r)(\alpha_{6061} - \alpha_{TiB_2})V_p}{bd_p(1 - V_p)}} \quad (10)$$

where the parameters are the same as the above-mentioned parameters, T_m is the temperature of casting, T_r is the temperature of the room, α_{6061} is the CTE value of the 6061 alloy ($23.6 \times 10^{-6} \cdot K^{-1}$) and α_{TiB_2} is the CTE value of TiB₂ particles ($8.3 \times 10^{-6} \cdot K^{-1}$). CTE strengthening is the main mechanism of the composites. The value of 6061 alloy deformation is much larger than that of TiB₂ particles, which leads to higher dislocation density around TiB₂ particles.

4.3. Wear Mechanisms

There are two wear mechanisms in the composites: adhesive wear and abrasive wear. As the wear pair slid relative to the composites, plastic deformation occurred in the composites under external load. The adhesive point formed by the adhesive effect undergoes shear fracture. In the beginning, the wear pair contacted the oxide layer on the surface of the composites. The oxide layer was sheared and destroyed, separated from the composites in the form of grinding debris. The exposed TiB₂ particles served as contact peaks with the wear pair. The hardness of TiB₂ particles is obviously higher than that of the 6061 alloy. At the sliding speed set in the test, the contact peaks have to withstand extremely high contact pressure and release high heat. However, due to the larger volume of the grinding pair than the contact peak point, if it is out of contact, the temperature will decrease rapidly. The adhesive wear volume within the total sliding distance can be calculated by Equation (11) [34,35]:

$$V = \frac{\alpha Fl}{H} \quad (11)$$

where V is the adhesive wear volume within the total sliding distance (mm³); α is a constant, related to the cleanliness and contact of the two wearing parts; F is the normal load (N); l

is the total sliding distance (mm); and H is the hardness of the composites (HB). Table 3 shows the hardness of the composites. The volume of adhesive wear of the composites is negatively correlated to the hardness of the composites. The 0.3 wt.%La-3 wt.%TiB₂ composites have the highest hardness, corresponding to the best wear resistance.

Table 3. The hardness of the composites with different La contents.

La content (wt.%)	0	0.1	0.3	0.5
Hardness (HB)	81.2 ± 0.1	83.5 ± 0.1	90.1 ± 0.2	78.2 ± 0.1

With abrasive wear, TiB₂ particles may separate from the composites, causing serious damage to the surface and leaving deeper pits on the surface. In the 3 wt.% TiB₂/6061 composites, there are serious particle agglomerations, which may separate during wearing. The abrasive wear volume within the total sliding distance can be calculated by Equation (12) [34,36]:

$$V = \frac{KFltg\theta}{H} \quad (12)$$

where the parameters are the same as the above-mentioned parameters; K is the friction coefficient, related to the shape of the abrasive particles; and $tg\theta$ is a geometric property factor, which is affected by the roughness of the contact surface. It can be known from Equation (12) that along with the hardness factor, the shape of the abrasive particles is another main factor affecting the wear resistance of the composites. As mentioned before, the addition of La changed the TiB₂ particle morphologies; many chamfering planes appeared on the particles rather than sharp edges. This would reduce the secondary damage to the composites caused by the sliding of TiB₂ particle agglomerations on the surface.

5. Conclusions

In this work, 3 wt.%TiB₂/6061 composites with different La contents were successfully fabricated by a salt–metal reaction route at 850 °C. The effects of different La contents on the microstructure, mechanical properties and friction behaviors of composites were investigated. The main conclusions drawn are as follows:

- (1) In 3 wt.%TiB₂/6061 composites, the average size of α -Al grains was about 150 μ m, and the agglomeration of TiB₂ particles was serious. With 0.3 wt.% La addition, the size of α -Al grains was refined, and the particle agglomeration was alleviated. The refinement of grain size could be attributed to the combined effect of La and TiB₂ particles. However, 0.5 wt.% La addition resulted in the coarsening of the α -Al grains.
- (2) The addition of La changed the ultimate morphologies of TiB₂ particles. In 0.3 wt.%La-3 wt.%TiB₂/6061 composites, TiB₂ particles maintained the basis of hexagonal prism morphology, with chamfering planes. The adsorption of La inhibited the growth of {11 $\bar{2}$ 0}, {1 $\bar{2}$ 12} and {10 $\bar{1}$ 1} crystal planes, leading to incomplete degeneration.
- (3) The in situ synthesized TiB₂/6061 composites with 0.3 wt% La show the best tensile property and good elongation. Compared with 3 wt.%TiB₂/6061 composites, the YS and UTS of 0.3 wt.%La-3 wt.%TiB₂/6061 composites increased 69.2% and 34.8%, and the EL increased by 5.7%.
- (4) The wear resistance of composites improved with trace La addition, and 0.3 wt.% La had the greatest effect on wear resistance. The average friction coefficient of the 0.3 wt.%La-3 wt.%TiB₂/6061 composites was the smallest, the curves were the smoothest, and the smallest and shallowest grooves were on the wearing surface. Adhesive wear and abrasive wear mechanisms existed in the friction behaviors of the composites.

Author Contributions: Conceptualization, W.Z.; methodology, J.J. and W.Z.; software, J.J. and J.L. (Jinghui Li) and Q.C.; validation, J.L. (Jingfu Liu); formal analysis, J.J., J.L. (Jinghui Li) and Q.C.;

investigation, J.J.; resources, W.Z. and J.L. (Jingfu Liu); data curation, J.J.; writing—original draft preparation, J.J.; writing—review and editing, W.Z.; visualization, W.Z.; supervision, J.L. (Jingfu Liu); project administration, J.L. (Jingfu Liu); funding acquisition, W.Z. All authors have read and agreed to the published version of the manuscript.

Funding: This research was funded by the Scientific Research Foundation of the Educational Department of Liaoning Province for Basic Research (CN) (No. LJKMZ20220670).

Data Availability Statement: The original contributions presented in the study are included in the article; further inquiries can be directed to the corresponding author.

Conflicts of Interest: The authors declare no conflict of interest.

References

1. He, Z.; Wang, J.; Zhu, M.; Wen, T.; Yang, F.; Ji, S.; Zheng, J.; Yang, H. Effects of In Situ TiB₂ on the Microstructural Evolution, Mechanical Properties, and Friction Behavior of the Al-Si-Cu Alloys Processed by Laser Powder-Bed Fusion. *Metals* **2024**, *14*, 1015. [[CrossRef](#)]
2. Jia, C.; Xu, Z.; Li, Y.; He, Y.; Liu, H.; ZHu, Z.; Liu, H.; Liu, C. Hot deformation behavior and microstructural evolution of an in-Situ 2 wt.% TiB₂-Reinforced 6061 Al matrix composite. *J. Mater. Eng. Perform.* **2024**, *33*, 3309–3319. [[CrossRef](#)]
3. Ma, X.; Yang, H.; Dong, B.; Shu, S.; Wang, Z.; Shao, Y.; Jiang, Q.; Qiu, F. Novel method to achieve synergetic strength–ductility improvement of Al-Cu alloy by in situ TiC-TiB₂ particles via direct reaction synthesis. *Mater. Sci. Eng. A* **2023**, *869*, 144810. [[CrossRef](#)]
4. Matveev, A.; Promakhov, V.; Schulz, N.; Vladislav, B.; Timur, T. Nano- and Submicron-Sized TiB₂ Particles in Al-TiB₂ Composite Produced in Semi-Industrial Self-Propagating High-Temperature Synthesis Conditions. *Metals* **2024**, *14*, 511. [[CrossRef](#)]
5. Dorri, M.; Omrani, E.; Lopez, H.; Zhou, L.; Yongho, S.; Rohatgi, P. Strengthening in hybrid Alumina-Titanium diboride Aluminum matrix composites synthesized by ultrasonic assisted reactive mechanical mixing. *Mater. Sci. Eng. A* **2017**, *702*, 312–321. [[CrossRef](#)]
6. Wu, L.; Li, X.; Han, G.; Deng, Y.; Ma, N.; Wang, H. Precipitation behavior of the high-Li-content in-situ TiB₂/Al-Li-Cu composite. *Mater. Charact.* **2017**, *132*, 215–222. [[CrossRef](#)]
7. Chen, F.; Chen, Z.; Mao, F.; Wang, T.; Cao, Z. TiB₂ reinforced aluminum based in situ composites fabricated by stir casting. *Mater. Sci. Eng. A* **2015**, *625*, 357–368. [[CrossRef](#)]
8. Yang, L.; Zhang, H.; Zhao, X.; Liu, B.; Chen, X.; Zhou, L. Study on the Microscopic Mechanism of the Grain Refinement of Al-Ti-B Master Alloy. *Metals* **2024**, *14*, 197. [[CrossRef](#)]
9. Gao, Q.; Wu, S.; Lü, S.; Xiong, X.; Du, R.; An, P. Improvement of particles distribution of in-situ 5 vol% TiB₂ particulates reinforced Al-4.5Cu alloy matrix composites with ultrasonic vibration treatment. *J. Alloys Compd.* **2017**, *692*, 1–9. [[CrossRef](#)]
10. Wu, Y.; Liu, B.; Kang, H.; Guo, E.; Li, J.; Du, G.; Chen, Z.; Wang, T. Ultrasound-assisted dispersion of TiB₂ nanoparticles in 7075 matrix hybrid composites. *Mater. Sci. Eng. A* **2022**, *840*, 142958. [[CrossRef](#)]
11. Agrawal, S.; Ghose, A.; Chakrabarty, I. Effect of rotary electromagnetic stirring during solidification of in-situ Al-TiB₂ composites. *Mater. Design.* **2017**, *113*, 195–206. [[CrossRef](#)]
12. Xie, H.; Cao, Y. Effect of holding time and Ti/B molar ratio on microstructure and mechanical properties of in-situ TiB₂/Al composites fabricated by mixed salt reaction. *Mater. Res. Express.* **2023**, *10*, 046511. [[CrossRef](#)]
13. Xue, J.; Wu, W.; Ma, J.; Huang, H. Study on the fabrication of in-situ TiB₂/Al composite by electroslag melting. *Sci. Eng. Compd. Compos. Mater.* **2021**, *28*, 73–82. [[CrossRef](#)]
14. Huang, J.; Xiang, Z.; Tang, Y.; Li, J.; Shen, G.; Shi, G.; Ma, X.; Chen, Y.; Chen, Z. Interfacial precipitation of the in-situ TiB₂-reinforced Al-Zn-Mg-Cu-Zr composite. *Mater. Chem. Phys.* **2023**, *301*, 127561. [[CrossRef](#)]
15. Yang, H.; Cai, Z.; Zhang, Q.; Shao, Y.; Dong, B.; Xuan, Q.; Qiu, F. Comparison of the effects of Mg and Zn on the interface mismatch and compression properties of 50 vol% TiB₂/Al composites. *Ceram. Int.* **2021**, *47*, 22121–22129. [[CrossRef](#)]
16. Wang, T.; Zheng, Y.; Chen, Z.; Zhao, Y.; Kang, H. Effects of Sr on the microstructure and mechanical properties of in situ TiB₂ reinforced A356 composite. *Mater. Design.* **2014**, *64*, 185–193. [[CrossRef](#)]
17. Zhang, T.; Feng, K.; Li, Z.; Kokawa, H. Effects of rare earth elements on the microstructure and wear properties of TiB₂ reinforced aluminum matrix composite coatings: Experiments and first principles calculations. *Appl. Surf. Sci.* **2020**, *530*, 147051. [[CrossRef](#)]
18. Huang, D.; Yan, D.; Ma, S.; Wang, X. Scandium on the formation of in situ TiB₂ particulates in an aluminum matrix. *J. Mater. Res.* **2018**, *33*, 2721–2727. [[CrossRef](#)]
19. Sun, J.; Wang, X.; Chen, Y.; Wang, F.; Wang, H. Effect of Cu element on morphology of TiB₂ particles in TiB₂/Al-Cu composites. *T. Nonferr. Metal. Soc.* **2020**, *30*, 1148–1156. [[CrossRef](#)]
20. Zhang, X.; Hu, J.; Dong, B.; Li, X.; Kou, S.; Zhang, S.; Qiu, F. Effect of Cu and Zn elements on morphology of ceramic particles and interfacial bonding in TiB₂/Al composites. *Ceram. Inter.* **2022**, *48*, 25894–25904. [[CrossRef](#)]
21. Xue, J.; Wu, W.; Ma, J.; Huang, H.; Zhao, Z. Study on the effect of CeO₂ for fabricating in-situ TiB₂/A356 composites with improved mechanical properties. *Mater. Sci. Eng. A* **2020**, *786*, 139416. [[CrossRef](#)]
22. Zhuang, W.; Jia, J.; Liu, J.; Qin, L.; Li, J.; Meng, C. Microstructure evolution and properties improvement of in-situ TiB₂/6061 composites via trace Mn addition. *J. Mol. Struct.* **2024**, *1301*, 137423. [[CrossRef](#)]

23. Jiang, H.; Zheng, Q.; Song, Y.; Li, Y.; Li, S.; He, J.; Zhang, L.; Zhao, J. Influence of minor La addition on the solidification, aging behaviors and the tensile properties of Al-Mg-Si alloys. *Mater. Charact.* **2022**, *185*, 111750. [[CrossRef](#)]
24. Tsai, Y.; Chou, C.; Lee, S.; Lin, C.; Lin, J.; Lim, S. Effect of trace La addition on the microstructures and mechanical properties of A356 (Al-7Si-0.35Mg) aluminum alloys. *J. Alloys Compd.* **2009**, *487*, 157–162. [[CrossRef](#)]
25. Zheng, Q.; Zhang, L.; Jiang, H.; Zhao, J.; He, J. Effect mechanisms of micro-alloying element La on microstructure and mechanical properties of hypoeutectic Al-Si alloys. *J. Mater. Sci. Technol.* **2020**, *47*, 142–151. [[CrossRef](#)]
26. Zhuang, W.; Yang, H.; Yang, W.; Cui, J.; Huang, L.; Wu, C.; Liu, J.; Sun, Y.; Meng, C. Microstructure, tensile properties, and wear resistance of in situ TiB₂/6061 composites prepared by high energy ball milling and stir casting. *J. Mater. Eng. Perform.* **2021**, *30*, 7730–7740. [[CrossRef](#)]
27. James, T.; Hemmingson, S.; Sellers, J.; Campbell, C. Calorimetric measurement of adsorption and adhesion energies of Cu on Pt (111). *Surf. Sci.* **2017**, *657*, 58–62. [[CrossRef](#)]
28. Wang, M.; Chen, Z.; Chen, D.; Wu, Y.; Li, X.; Ma, N.; Wang, H. The constitutive model and processing map for in situ 5 wt.% TiB₂ reinforced 7050 Al alloy matrix composite. *Key. Eng. Mater.* **2014**, *575*, 11–19. [[CrossRef](#)]
29. Sun, G.; Zhao, G.; Shao, L.; Li, X.; Deng, Y.; Wang, H. Particle dispersion and mechanical properties enhancement of in-situ TiB₂/7050 Al matrix composite via additive friction stir deposition. *Mater. Lett.* **2024**, *357*, 135790. [[CrossRef](#)]
30. Bian, Z.; Cai, Y.; Zhang, D.; Wu, Y.; Zhao, D.; Wang, M.; Cui, S.; Wang, H. Improving mechanical performance of heat-resistant eutectic Al-Fe-Ni alloy by in-situ TiB₂ particles. *Mater. Lett.* **2024**, *358*, 135857. [[CrossRef](#)]
31. Zhuang, W.; Qin, L.; Jia, J.; Li, J.; Cao, Q.; Meng, C.; Liu, J. Microstructure and mechanical properties of network/point cluster structured TiC/6061 composites prepared by in-situ synthesis. *Mater. Lett.* **2024**, *365*, 136446. [[CrossRef](#)]
32. Ding, W.; Cheng, Y.; Taili, C.; Zhao, X.; Liu, X. Research status and application prospect of Aluminum matrix composites. *Res. Appl. Mater. Sci.* **2020**, *2*, 74–92.
33. Liu, Z.; Dong, Z.; Cheng, X.; Zheng, Q.; Zhao, J.; Han, Q. On the supplementation of Magnesium and usage of ultrasound stirring for fabricating in situ TiB₂/A356 composites with improved mechanical properties. *Metal. Mater. Tran.* **2018**, *49*, 5585–5598. [[CrossRef](#)]
34. Hushan, B. *Introduction to Tribology*; Wiley: New York, NY, USA, 2002; p. 732.
35. Lu, H.; Zhu, P.; Wang, W. Study of adhesive wear mechanisms in asperity junctions based on phase field fracture method. *Mater. Today Comm.* **2024**, *40*, 109903. [[CrossRef](#)]
36. Poria, S.; Sutradhar, G.; Sahoo, P. Design of experiments analysis of friction behavior of Al-TiB₂ composite. *Mater. Today Proc.* **2017**, *4*, 2956–2964. [[CrossRef](#)]

Disclaimer/Publisher’s Note: The statements, opinions and data contained in all publications are solely those of the individual author(s) and contributor(s) and not of MDPI and/or the editor(s). MDPI and/or the editor(s) disclaim responsibility for any injury to people or property resulting from any ideas, methods, instructions or products referred to in the content.